Influence of Pore Size and Crystallography on the Small Crack HCF Behavior of an A357-T6 Cast Aluminum Alloy

I. SERRANO-MUNOZ, S. DANCETTE, C. VERDU, and J.-Y. BUFFIERE

The high-cycle fatigue, small crack propagation behavior of an A357-T6 cast aluminum alloy is investigated. Laboratory X-ray micro-computed tomography (μCT) is used to assist in the manufacturing of two flat fatigue specimens containing subsurface shrinkage pores of different sizes (Pore 1 $\sqrt{A} = 522\,\mu$m against Pore 2 $\sqrt{A} = 280\,\mu$m). Surface crack monitoring is performed by means of optical microscopy and the cracked specimens are analyzed *via* scanning electron microscopy and electron backscatter diffraction techniques. The subsurface pores tend to induce intergranular crack nucleation, principally when the grain boundaries are oriented perpendicular to the loading direction. Pore 1 induces a fatigue life reduction of 500.000 cycles when compared to Pore 2. The crystallography is able to influence small crack propagation by slightly decelerating the crack growth rates as well as by altering the crack path topography. Tailoring of the crystallography for improved fatigue resistance requires an investigation of the optimal largest defect to grain size ratio.

https://doi.org/10.1007/s11661-019-05590-6

I. INTRODUCTION

AlSi cast alloys appear as attractive solutions to the aerospace industry because of their lightweight and cost-effectiveness. Complex structural parts can be manufactured to final shape without a need for machining and/or assembly operations. Nonetheless, the poor fatigue resistance properties exhibited by these materials, particularly in the high-cycle fatigue domain (HCF, $10^5 < N_f < 10^7$ cycles),[1–15] limit their use to non-critical parts. Improving the fatigue resistance of cast parts is, therefore, paramount to promote their use as replacement for costly wrought solutions (manufactured using assembling and/or subtractive techniques), which are conventionally used in critical parts.

The total fatigue life N_T of a component can be divided into:

$$N_T = N_I + N_P, \quad [1]$$

where N_I is the number of cycles to initiate a dominant crack which size is larger than the intrinsic microstructural features (*i.e.*, grains or phases). N_P is the number of cycles of propagation until the occurrence of final failure.[16–18] The duration of N_P can be calculated using linear elastic fracture mechanics concepts and long crack (LC) growth data. The determination of N_I is more complicated and numerous approaches have been proposed. Moreover, a detailed decomposition of N_I has been introduced as follows[19]:

$$N_I = N_N + N_{MSC} + N_{PSC}, \quad [2]$$

where N_N is the number of cycles needed to nucleate a crack embryo, N_{MSC} is the number of cycles of propagation in the microstructurally small cracks (MSCs) regime and N_{PSC} is the propagation in the physically small cracks (PSCs) regime.[19] During the N_{MSC} period, the microstructure highly influences crack growth rates by slowing down and sometimes even arresting crack propagation for numerous cycles.[20–25] At N_{PSC}, cracks are large enough to be no longer influenced by the microstructural features although their crack-tip plastic zone is not sufficiently developed to induce crack closure effects. In HCF conditions, the extent of N_I can be significantly affected by microstructural features and defects.[26,27]

It has been reported that the initiation and propagation of a micro-crack up to 1 mm in length accounts for about 90 pct of the total fatigue life in a material considered defect free.[28] Thus, there are different degrees of pore harmfulness depending on its ability to

---

I. SERRANO-MUNOZ is with the Université de Lyon, INSA-Lyon, MATEIS CNRS UMR 5510, Villeurbanne 69621 Cedex, France and also with the Bundesanstaltfür Materialforschung und -prüfung (BAM), Unter den Eichen 87, 12205, Berlin, Germany. Contact e-mail: itziar.serrano.munoz@gmail.com S. DANCETTE, C. VERDU, and J.-Y. BUFFIERE are with the Université de Lyon. Contact email: jean-yves.buffiere@insa-lyon.fr

Manuscript submitted on July 3, 2019.

reduce or even suppress N_{I} period.[1–15] Note that the pore harmfulness depends on several parameters such as the size,[29] morphology,[30] and location (*i.e.*, surface, subsurface or internal pores[31]). If the pore is harmful enough (*e.g.*, 1 mm located at the free surface), N_{I} will be drastically reduced. Intermediate harmfulness is thought to mainly reduce/suppress N_{N}, with N_{MSC} being influenced to different extends depending on the adjacent microstructure. There is a critical condition below which pores are no longer able to propagate cracks (although they might nucleate non-propagating cracks, as shown in Reference [6]). In this case, the role of limiting fatigue life is passed down to other microstructural features such as the secondary dendrite arm spacing (SDAS) and intermetallics. For instance, it has been observed[32] that a SDAS reduction (from 70 to 30 μm) leads to increased fatigue lives (case of a pore-free A356-T6 cast alloy).

Since the SDAS is considered to be the microstructural parameter controlling crack propagation within N_{MSC},[33] no particular attention is given in the literature to the influence of crystallography on nucleation and small crack propagation. Nevertheless, it has been observed, for example, that increasing the average grain size in a 7475 aluminum alloy leads to enhanced crack path roughness, intensifying crack closure effects.[34]

Thus, the present work focuses on the role played by pore size and local microstructure in the duration of N_{I}, with special attention paid to the crystallographic features (*i.e.*, size, orientation and grain boundaries). Prior to fatigue testing, the presence of pores within the gage volume is controlled by laboratory micro-computed tomography (μCT) means. Crack nucleation and propagation is monitored with light optical microscopy and the crystallography is investigated by performing electron backscatter diffraction (EBSD) analyses on the cracked specimens. The most relevant results are presented and the influence that pore size, SDAS, and neighboring crystallography have on the nucleation and propagation of small cracks is examined in detail.

II. MATERIAL AND METHODS

A. *Material*

The studied A357-T6 cast aluminum alloy was provided in the form of $\varnothing 30 \times 250$ mm rods. The heat treatment consisted of (a) solution treatment at 540 °C for 10 h in an air circulated furnace; (b) water quenching at room temperature; and (c) artificially aging to the peak age condition at 160 °C for 8 h. The chemical composition (wt pct) is as follows: 6.94 Si, 0.56 Mg, 0.097 Fe, 0.13 Ti, $<$ 0.015 Cu, $<$ 0.03 Mn, and $<$ 0.003 Pb, balance Al. Regarding the mechanical parameters, the modulus of elasticity is 73.5 GPa, and the yield strength is $\sigma_{\mathrm{YS}} = 275$ MPa, the ultimate tensile strength is $\sigma_{\mathrm{UTS}} = 335$ MPa, and the elongation percentage at fracture is 6 pct.

For all samples used in quantitative metallography (both optical and EBSD), the region of interest (ROI) is a 10 mm × 10 mm area located at the center of the rods. The size of eutectic Si particles was evaluated using 20 optical microscopy micrographs at ×20 magnification, where the plug-in *Analyze Particles* available on the free software Fiji™[35] was applied after thresholding. The average Feret's diameter* is $L_{\mathrm{Si}} = 4 \pm 3\,\mu$m. Measurement of the SDAS was carried out following the ARP1947B Standard.[36] SDAS was obtained by identifying and measuring aligned groups of secondary dendrite cells. The value of the SDAS was then calculated as $\mathrm{SDAS} = AB/nM$, where AB is the length of the line drawn from edge to edge of the measured dendrite. M is the magnification and n the number of dendrite cells crossed by the line (n has to be at least 5 or larger). 155 Measurements performed on 50 micrographs at ×10 yielded and average spacing of $\mathrm{SDAS} = 38 \pm 6\,\mu$m.

Optimum sample preparation is crucial to obtain an adequate indexing rate during EBSD analysis. AlSi cast alloys are particularly *difficult* to prepare, as the soft Al-α matrix is easily strained in depth and tends to get scratched by the harder Si phase. Therefore, the preparation process needed to be done manually, using low rotation speed while simultaneously applying a soft pressure onto the samples. Sample preparation consisted of mechanical grinding from P1200 down to P4000 grit papers, using intermediate P2500 paper. This was followed by polishing on cloth using a diamond particle suspension of 9 μm for at least 5 minutes followed by another 5 minutes of polishing with 3 μm diamond suspension. Final fine polishing was performed using 0.02 μm non-crystallizing colloidal silica suspension for not more than 3 minutes.

Crystallographic orientations were determined using an EBSD system installed in a ZEISS SUPRA™ 55 VP scanning electron microscope (SEM) equipped with HKL technology Channel 5.0 and AZtecHKL data acquisition.[37] The SEM was operated at an accelerating voltage of 20 kV with a working distance of 13 mm. Seven EBSD maps of $\sim 5\,\mathrm{mm} \times 5\,\mathrm{mm}$ maps were collected with a step size of 5 μm. Neighboring pixels with disorientation larger than 5 deg were considered to belong to different grains. The grain size was defined using the equivalent spherical diameter** ($\varnothing_{A_{eq}}$). A total of 1416 grains (excluding the grains that resided at the border of the EBSD image) were used to perform an area fraction analysis of the average grain size,† which led to $\varnothing_{A_{\mathrm{eq}}} = 501\,\mu$m.

---

*The longest distance between any two points a particle.

**A circle having the same Area as the measured grain ($\varnothing_{A_{eq}} = \sqrt{\frac{4 \times Area}{\pi}}$).

†The average grain size was calculated using a weighted arithmetic average where the largest grains contribute more to the final average than the smallest.

Laboratory X-ray μCT was performed using a Phoenix V||Tome||X system. For each sample, 1801 projections were collected *via* a 2000 pixel-wide detector and an acquisition time of 500 ms per radiography. The X-ray source operated at a tube voltage of 80 keV and an intensity of 90 μA. The relative source, sample, and detector distances, with no pixel binning, gave a native voxel size of $(12\,\mu\text{m})^3$. Seven samples of $\varnothing$6x25mm^3 were examined to obtain a representative sampling of the pore population. The size of each individual pore was defined as the diameter $\varnothing_{V_{\text{eq}}}$ of a sphere having the same volume as the measured pore $\left(\varnothing_{V_{\text{eq}}} = \left(\frac{6\times\text{Volume}}{\pi}\right)^{\frac{1}{3}}\right)$. The largest pores (considered as those with sizes larger than $\varnothing_{V_{eq}} = 100\,\mu$m) only represents 2 to 3 pct of the total counts of the distribution. The average pore volume fraction is $f = 0.002$ pct. More details about the microstructural characterization of this material can be found in Reference 38.

B. *Fatigue Testing*

The above laboratory μCT evaluation of porosity content indicates that the material of study is relatively sound. This means that the location of early crack nucleation is most certainly known if one of these *large* pores happen to be intercepting (or immediately beneath) the free surface. Hence, six specimens (two per rod) were carved out of the center of the as-received rods using electrical discharge machining (EDM). The geometry of the fatigue specimens is given in Figure 1. After EDM and prior to the EBSD grinding and polishing processes, the specimens are scanned using laboratory μCT in order to *control* the location of large pores within the gage. A specimen was selected for fatigue testing when it contained at least one large pore ($\varnothing_{V_{eq}} > 100\,\mu$m). When needed, mechanical grinding using P500 grit paper was performed in order to bring the controlled pores to intercept the free surface. Note that crack monitoring is performed only on one of the frontal surfaces.

After the EBSD grinding/polishing and prior to fatigue testing, the selected specimens are, again, scanned using laboratory μCT to determine the final dimensions of the controlled pores. These pores, considered as the most favorable sites for early crack nucleation, were monitored throughout the entire experiment using optical microscopy.

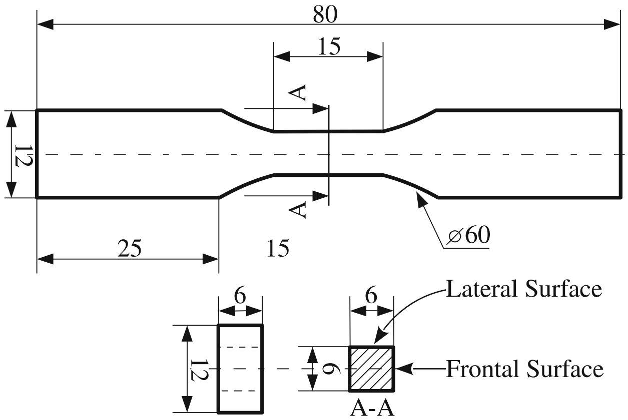

Fig. 1—Geometry of fatigue specimens used for surface crack monitoring (dimensions in millimeters).

Fatigue testing was performed using a servo-hydraulic Instron-8516 machine at a frequency of 10 Hz and $R = 0.1$. The remote load was $\sigma_{\max} = 163$ MPa and images of the crack propagation were recorded at intervals of 50.000 cycles for the first stages of propagation, reducing the intervals to 10.000 cycles when the cracks reached ~ 1 mm length. At $\sigma_{\max} = 163$ MPa, the Wöhler curve indicates a life expectancy of $N_{\text{T}} = 500.000$ cycles. Experiments were stopped when the surface cracks reached a length of ~ 2 mm (*i.e.*, about four times the average surface grain size).

Apart from the study of grain boundaries and crystal orientations, the EBSD data were used to investigate stress concentration and the Taylor slip activity ($\dot{\gamma}^{\text{s}}$) of each potential $111\langle 110\rangle$ slip system. The Taylor model[39–42] assumes iso-deformation of all grains and does, therefore, not consider intergranular stress and strain interactions. Such calculation of the heterogeneity of the mechanical fields in the polycrystal can be assessed by full-field crystal plasticity finite element modeling (CPFEM). The procedure used in this study is described in detail in Reference 43 and briefly recalled here. Grains in the EBSD map were identified using a 10-deg disorientation threshold. Grain boundaries and triple points were automatically extracted from the grain map in order build a 2D finite element model that conforms to grain boundaries. The 2D mesh was subsequently extruded in the third direction to produce a thin 3D mesh of prismatic elements in which out-of-plane boundary conditions can be easily controlled. The measured crystallographic orientation of the corresponding grain in the map was then attributed to each finite element of the mesh. The finite element simulation was run assuming plane stress, which is motivated by the free surface analyses by EBSD. The upper surface of the grain map is uniformly displaced in order to produce a small tensile strain of 1 pct, qualitatively mimicking the applied fatigue stress state. The elasto-viscoplastic crystal plasticity user subroutine developed in Abaqus (described in References 41 and 44) computes the multiplicative decomposition of the imposed FE deformation gradient and allows to evaluate the corresponding shear rates on all 12 $111\langle 110\rangle$ slip systems along with the corresponding stress state $\boldsymbol{\sigma}$ in the element. The shear rate $\dot{\gamma}^{\text{s}}$ on slip system s was computed as a power law depending on the resolved shear stress $\tau^{\text{s}} = (\boldsymbol{b}^{\text{s}} \otimes \boldsymbol{n}^{\text{s}}) : \boldsymbol{\sigma}$ on that slip system (unit normal $\boldsymbol{n}^{\text{s}}$ and unit slip direction $\boldsymbol{b}^{\text{s}}$):

$$\dot{\gamma}^{\text{s}} = \dot{\gamma}_0 \left|\frac{\tau^{\text{s}}}{\tau_{\text{c}}^{\text{s}}}\right|^{1/m} \text{sign}(\tau^{\text{s}}), \qquad [3]$$

where $\dot{\gamma}_0 = 0.001$ is a reference slip rate, $m = 0.05$ is the strain-rate sensitivity exponent and $\tau_{\text{c}} = 100$ MPa is the critical resolved shear stress that must be reached for observing significant activity on that system. This set of parameters was chosen to ensure that the onset of plasticity occurs at a tensile stress level corresponding to the material YS level, with a low strain-rate sensitivity. Knowing the stress state $\boldsymbol{\sigma}$ and the shear rates allowed to compute the slip traces of the most activated slip systems on the observation surface. The procedure to automatize the representation of the traces of preferential slip systems in each grain is described in Reference 45.

III. RESULTS

Only two specimens were found suitable for fatigue testing after the laboratory μCT screening (Samples A and B hereafter). Figure 2(a) shows the 3D morphology of the pore (named Pore 1) contained in Sample A. The square root of the pore surface ($\sqrt{A}$[29]) projected along the loading axis Z is used to measure the size of defects. Here, the ligament[‡] between the pore and the free surface is included in the measurement of the projected area (see Figure 2(b)). Thus, the size of Pore 1 is considered to be $\sqrt{A} = 522\,\mu$m. Likewise, Figure 2(c) shows the 3D morphology of the pores contained in Sample B, where Pore 2 is also shown in dark magenta and Pore 3 in pink. Pore 2 is half the size of Pore 1 ($\sqrt{A} = 280\,\mu$m, Figure 2(d)) and the size of Pore 3 is $\sqrt{A} = 73\,\mu$m.

A. *Crack Monitoring*

Figures 3(a) through (c) shows the most relevant stages of crack propagation within Sample A. Three cracks (named c_{l1}, c_{r1}, and c_{l2}) are already initiated after $N_{\mathrm{T}} = 50.000$ cycles (Figure 3(a)). The sum of c_{l1} and c_{r1} is hereafter referred as Crack A and its length at this stage is $2c = 586\,\mu$m (instead of the full-path length, the $2c$ parameter is measured considering the projection of the crack along the Z direction). c_{l2} crack was arrested at some point between 0 and 50.000 cycles, as propagation is no longer observed in the subsequent recorded stages. At 150.000 cycles, Crack A has doubled its size and c_{l1} has bifurcated into c_{l3} before being arrested (Figure 3(b)). Another bifurcation before arresting (c_{r1} into c_{r2}) occurred between 150.000 and 180.000 cycles (Figure 3(c)). The final length is $2c = 2160\,\mu$m and the crack path topography can be considered as flat and mostly perpendicular to the loading direction, with no signs of slip grooves characteristic of crystallographic propagation.

Sample B exhibits three micro-cracks ($\sim 50\,\mu$m) at $N_{\mathrm{T}} = 50.000$ cycles (*i.e.*, $\sim$ 10 pct of the expected fatigue life, see Figure 3(d)). Two of them (c'_{l1} and c'_{r1}) are nucleated at Pore 2 while the third crack (c'_{r2}) is nucleated at Pore 3. This last crack is arrested at $\sim$ 150.000 cycles and never resumes propagation. c'_{r3} is also arrested, in this case after $\sim$ 200.000 cycles (Figure 3(e)). There is an interval of cycles (from $N_{\mathrm{T}} = 400.000$ to 500.000 cycles) where only c'_{l1} crack is propagating. Finally, c'_{r4} crack is initiated between 500.000 and 550.00 cycles. The sum of c'_{l1} and c'_{r4} is hereafter referred as Crack B and its length at this stage is $2c = 558\,\mu$m. Crack B continues propagation until the experiment is stopped at $N_{\mathrm{T}} = 780.000$ cycles (Figure 3(f)). The final crack length is $2c = 2030\,\mu$m. Sample B also exhibits a flat crack path, although the roughness is considerably increased at the last stages of propagation, between $N_{\mathrm{T}} = 700.000$ and 780.000 cycles, where Crack B shows some serrated/crystallographic features.

Figure 4 shows the steady growth of Sample A crack (Crack A is shown in blue) from the initial $2c = 586\,\mu$m at 50.000 cycles until reaching 2160 μm at 210.000 cycles. The curve obtained for Sample B shows two different slopes where slow growth occurs until reaching $2c = 558\,\mu$m at 550.000 cycles. At this point, the crack starts

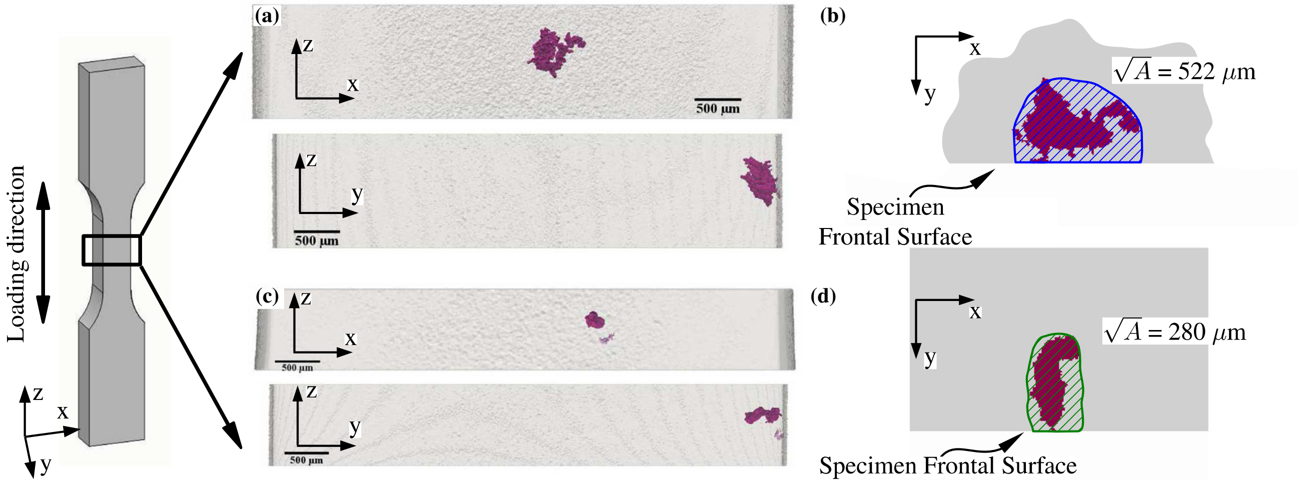

Fig. 2—(*a*) 3D rendering of Sample A gage where Pore 1 is shown in dark magenta. (*b*) Projection of Pore 1 along the Z loading direction. The hatched surface in blue is used to measure the $\sqrt{A}$ parameter. (*c*) 3D rendering of Sample B gage which contains two pores: Pore 2 shown in dark magenta and smaller Pore 3 shown in pink. (*d*) Surface projection of Pore 2 along the Z loading direction (Color figure online).

[‡] In this work, ligament is referred as the thin bridge of material standing between the specimen free surface and the subsurface pores.

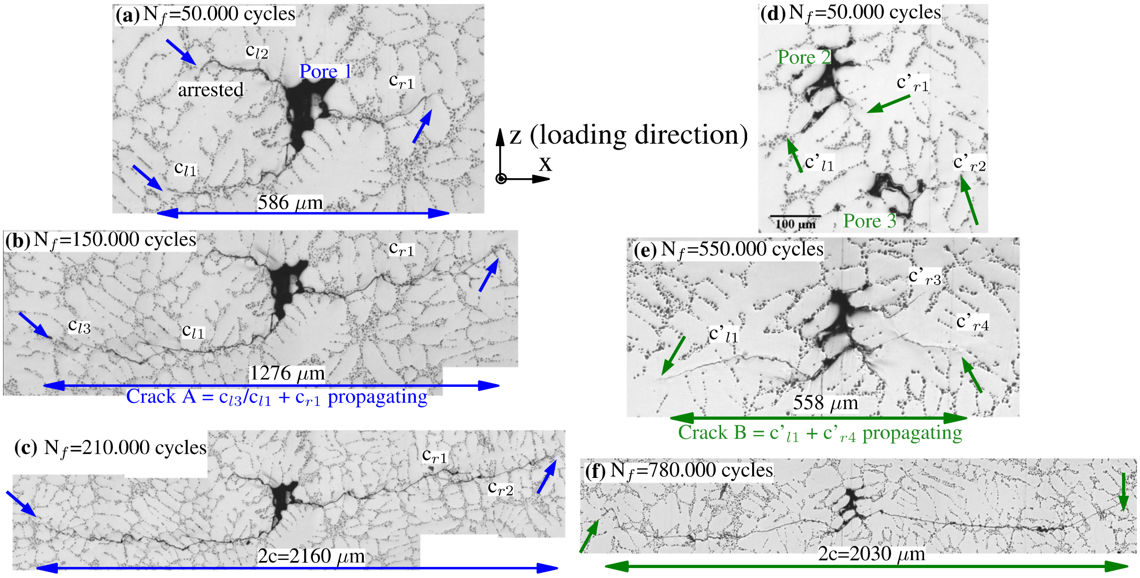

Fig. 3—Sequence of optical images showing crack propagation in Sample A at (*a*) $N_T = 50.000$ cycles, (*b*) $N_T = 150.000$ cycles, and the last recorded stage at (*c*) $N_T = 210.000$ cycles. Sample B crack propagation at (*d*) $N_T = 50.000$ cycles, (*e*) $N_T = 550.000$ cycles, and the last recorded stage at (*f*) $N_T = 780.000$ cycles. Arrows indicate the crack-tip position.

to propagate faster, exhibiting a slope similar to that of Sample A, which spans until 2030 μm at 780.000 cycles. Overall, Crack B needed 500.000 cycles more to be as long as Crack A was after 50.000 cycles.

B. *EBSD Analyses*

The influence of the crystallography and ligament on the first stages of small crack propagation ($N_{MSC} + N_{PSC}$) is investigated in Figure 5. Note that the crack nucleation period (N_N) is not precisely known because when the first images are recorded, after 50.000 cycles, well-developed propagating cracks are observed in both samples. For Sample A, Figure 5(a) shows that c_{r1}, c_{l1}, and c_{l2} cracks nucleated at convex zones of the pore following intergranular paths between Si eutectic particles. c_{r1} crack propagates for $c \approx 112\,\mu$m (measured as the projected length) before being deflected into intragranular growth. For c_{l1} crack, the deflection occurs at $c \approx 255\,\mu$m. The addition of Pore 1 underlying profile suggests that the intergranular crack propagation approximately corresponds to the presence of the subsurface pore. Because the first image is recorded when Crack A has already switched into intragranular propagation, it was not possible to determine if the crack growth rates decelerate when switching from inter to intragranular propagation. Pore 2 also nucleates cracks at convex zones, exhibiting some intergranular propagation (c'_{r1} and c'_{r2} cracks, Figure 5(b)) that, again, can be related to the presence of the subsurface region of Pore 2.

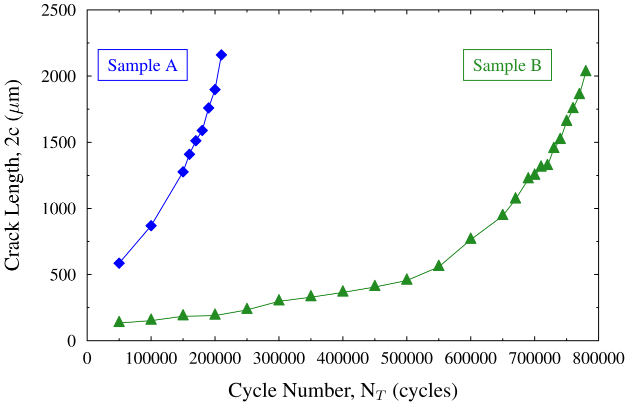

Fig. 4—Plot of the surface crack size (2*c*) against the number of cycles N_T. Sample A results are shown in blue diamonds and Sample B results are given in green triangles (Color figure online).

Figure 6 shows the combination of EBSD and crack propagation monitoring results for Sample A, where cracks are able to propagate for considerable lengths ($c_{l3} \approx 691\,\mu$m and $c_{r2} \approx 1125\,\mu$m) before encountering the first grain boundaries (Figures 6a and b). Moreover, some of the decelerations do not always correspond to cracks crossing grain boundaries. For instance, no slowing down is observed at the surface when the crack crosses the grain boundary between Grains 6 and 7 (Figure 6(c)), although the crack growth is decelerated within Grain 1 during the c_{r1}-to-c_{r2} bifurcation. Some deceleration is also observed when c_{l3} crack crosses Grain 7 subgrain boundary.

The number of grain boundaries crossed by Crack B before 780.000 cycles is higher than that of Crack A (five more, see Figures 7(a) and (b)). Crack B also propagated along considerable lengths ($c'_{l2} \approx 432\,\mu$m and $c_{r4} \approx 596\,\mu$m) before encountering the first grain boundaries. Crack growth decelerations related to the presence of grain boundaries also occur in this sample. Interestingly, crack propagation rates remain constant for almost half of the propagation occurring within Grain 13. It is also observed that the increase in crack path roughness occurring after 750.000 cycles is resulting from propagation through three different grains (Grains 13, 14, and 19).

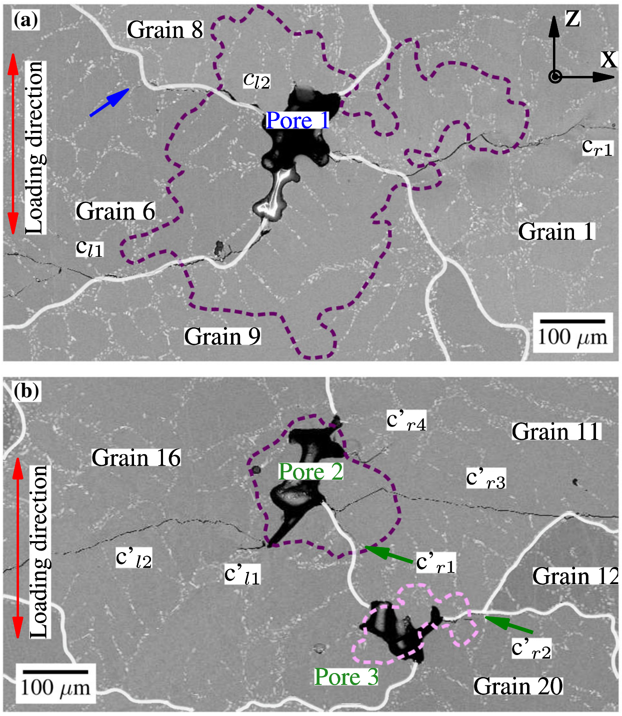

Fig. 5—(*a*) Backscattered electrons (BSE) image of Pore 1, where the grain boundaries are shown in white. The outline in dark magenta corresponds to the approximate location of the underlying region of Pore 1 obtained using μCT images. The blue arrow indicates the crack-tip position of c_{l2} crack. (*b*) BSE image where the outline in dark magenta corresponds to the approximate location of the underlying region of Pore 2 and the pink outline corresponds to Pore 3. The green arrows indicate the crack-tip position of c'_{r1} and c'_{r2} cracks. The remote stress is applied along *Z*-axis (Color figure online).

High-resolution SEM images on Grain 13 reveal the occurrence of a micro-serrated crack path (Figure 8(a)). In this grain, a series of crystallographic slip grooves are observed to alternate propagation between −61 deg (clockwise rotation is given negative values) and 66 deg. The entire propagation through across Grain 14 occurs on a single slip plane at 28 deg. Right before entering Grain 15, the crystallographic crack decelerates before branching into a non-crystallographic crack. Grain 19 (Figure 8(b)) also exhibits a serrated crack path, although in this case crystallographic propagation at −72 deg alternates with what appears as non-crystallographic propagation.

Note that the cracking of Si particles is not observed throughout both Cracks A and B. However, the cracking intermetallic particles can be observed at different propagation stages (see Figure 9). Moreover, intermetallic particles cracking is observed even when the particle is laying parallel to the crack propagation direction (Figure 9(b)) which indicates that Fe-rich intermetallic particles are more brittle than Si eutectic particles.

IV. DISCUSSION

Tomographic images show that the studied pores have convoluted morphologies characteristic of interdendritic shrinkage porosity. This type of porosity results from the volumetric shrinkage occurring during solidification. This is the reason why the pores observed in this study tend to be surrounded by grain boundaries,[46] as shown in Figures 6(a) and 7(a). Further, it could be argued that the presence of grain boundaries within the ligament has a weakening role, further reducing the resistance of this region to early cracking (see Figure 10).

As shown in Section III, both Pores 1 and 2 produce fatigue-limiting crack nucleation. Nevertheless, there is a significant difference in the numbers of cycles required to grow a micro-crack up to $2c, \approx 570\,\mu\text{m}$ (see Figures 3 and 4). The main difference between those two circumstances/cracks is the pore size. Pore 1 (Crack A) is almost twice the size of Pore 2 (Crack B). Another important difference is the twofold curve exhibited by Crack B (Figure 4). As proposed by Gall *et al.*,[33] the maximum size of the plastic zone at the different cycling stages is calculated using an Irwin-based approach [47]. For the crack shape, specimen geometry, and loading conditions introduced above, the maximum plastic zone size under plane stress conditions is estimated as:

$$r_y \approx \frac{1}{2\pi}\left(\frac{K_{\max}}{\sigma_y}\right)^2, \qquad [4]$$

where σ_y is the YS. The general solution for the maximum crack-tip driving force during tensile fatigue testing is:

$$K_{\max} = \beta\sigma_{\max}\sqrt{\pi c}, \qquad [5]$$

where β is a function of the specimen geometry and the loading configuration, $\sigma_{\max}$ is the maximum remote applied stress during the fatigue test, and a is the crack length toward the interior (*i.e.*, internal length) of the specimen. For the samples studied here, the stress intensity solution is obtained by considering the fatigue specimen as a flat plate containing a semi-elliptical centered flaw with a curvilinear crack front. The calculation of $K_{\max}$ depends on the 3D shape of the propagating crack.[48] Surface crack monitoring does not give information about the internal crack length parameter, a. However, synchrotron μCT combined with *in situ* fatigue testing[31] showed that, once the crack is out of the zone stress-influenced by the pore, the aspect ratio of the crack shape remains approximately constant at all recorded stages of propagation. Hence, the aspect ratio used in this study is $a/c = 1.1$ and the numerical solutions for β are taken from Reference 48.

The results of r_y after using Eq. [4] are shown in Table I. Note that the r_y calculation is a rough estimation, where numerous assumptions are considered. For instance, the calculation of r_y and $K_{\max}$ is skipped for

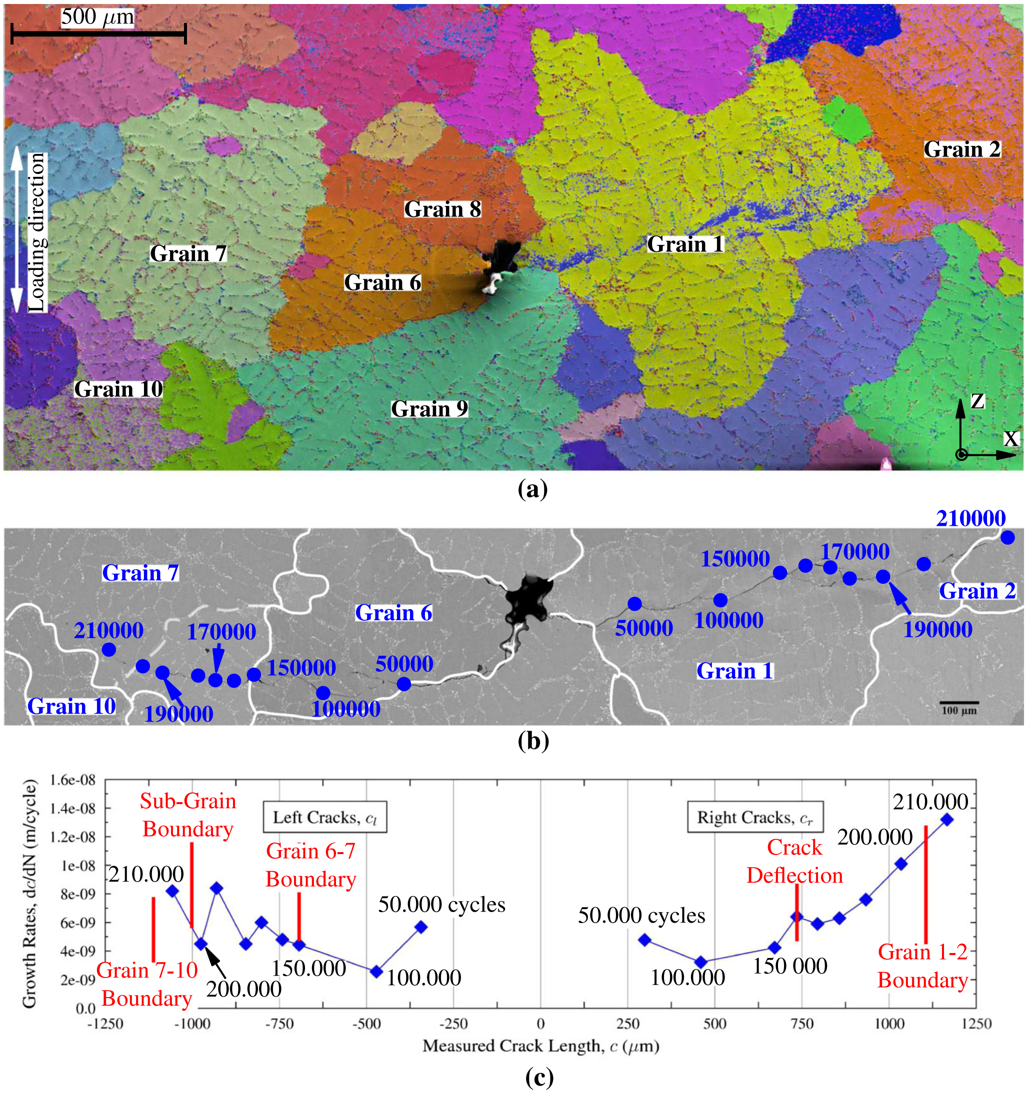

Fig. 6—(*a*) EBSD Euler map of the grain population of Sample A. The remote stress is applied along *Z*-axis. (*b*) BSE image of the crack path with blue circles indicating the recorded stages of propagation from 50.000 to 210.000 cycles. The white lines correspond to the approximate location of grain boundaries, and the dashed line corresponds to a subgrain boundary (lattice disorientation lower than 5 deg). (*c*) Plot of the crack growth rates $\mathrm{d}c/\mathrm{d}N$ against the measured crack lengths c.

Crack A at 50.000 cycles because, at this stage, the crack is considered to be influenced by the local stress field generated by Pore 1. This is not the case of Crack B which after 550.000 cycles is considered to be no longer influenced by Pore 2 (see Figures 3(e) and 5(b)).

Table 1 shows that the maximum values of $K_{\max}$ for the two studied cracks ($K_{\max} = 6.42\,\mathrm{MPa}\,\sqrt{m}$ for Sample A at 210.000 cycles and $K_{\max} = 6.22\,\mathrm{MPa}\,\sqrt{m}$ for Sample B at 780.000 cycles) are close to the $K_{\max}^{\mathrm{tr}} \approx 7\,\mathrm{MPa}\,\sqrt{m}$ threshold considered as the transition from Si particles being debonded at the crack-tip, to Si particles being fractured.[33] This result is consistent with the BSE observations (Figure 9) where no cracking of Si particles was observed at any point of the crack paths.

Table I also shows that the points where the crack-tip plastic zone r_y reaches the size of the SDAS (38 μm) corresponds to $\sim$ 100.000 cycles for Sample A ($r_y = 34.5\,\mu$m) and $\sim$ 650.000 cycles for Sample B ($r_y = 37.5\,\mu$m). Moreover, this latter point corresponds to the change in slope observed in Figure 4 and can be considered as the transition from MSC to PSC behavior. Note that this transition is not observed in Crack A, which only seems to undergo PSC propagation.

As mentioned in Section I, the variability of fatigue life is pronounced in the HCF regime. This variability highly depends on the size of the surface/subsurface defects. A classification based on the degree of harmfulness (*i.e.*, the defect size) can be established for the pores investigated in the present study:

- Pore 1 can be considered *large* enough to drastically reduce/suppress both N_{N} and N_{MSC} periods (see Figure 11(a)).
- Pore 2 is harmful to the fatigue life of the material but to a lesser extent. Its *intermediate* size reduces N_{N} period while still allowing MSC propagation to occur (see Figure 11(b)). Interestingly, at this pore

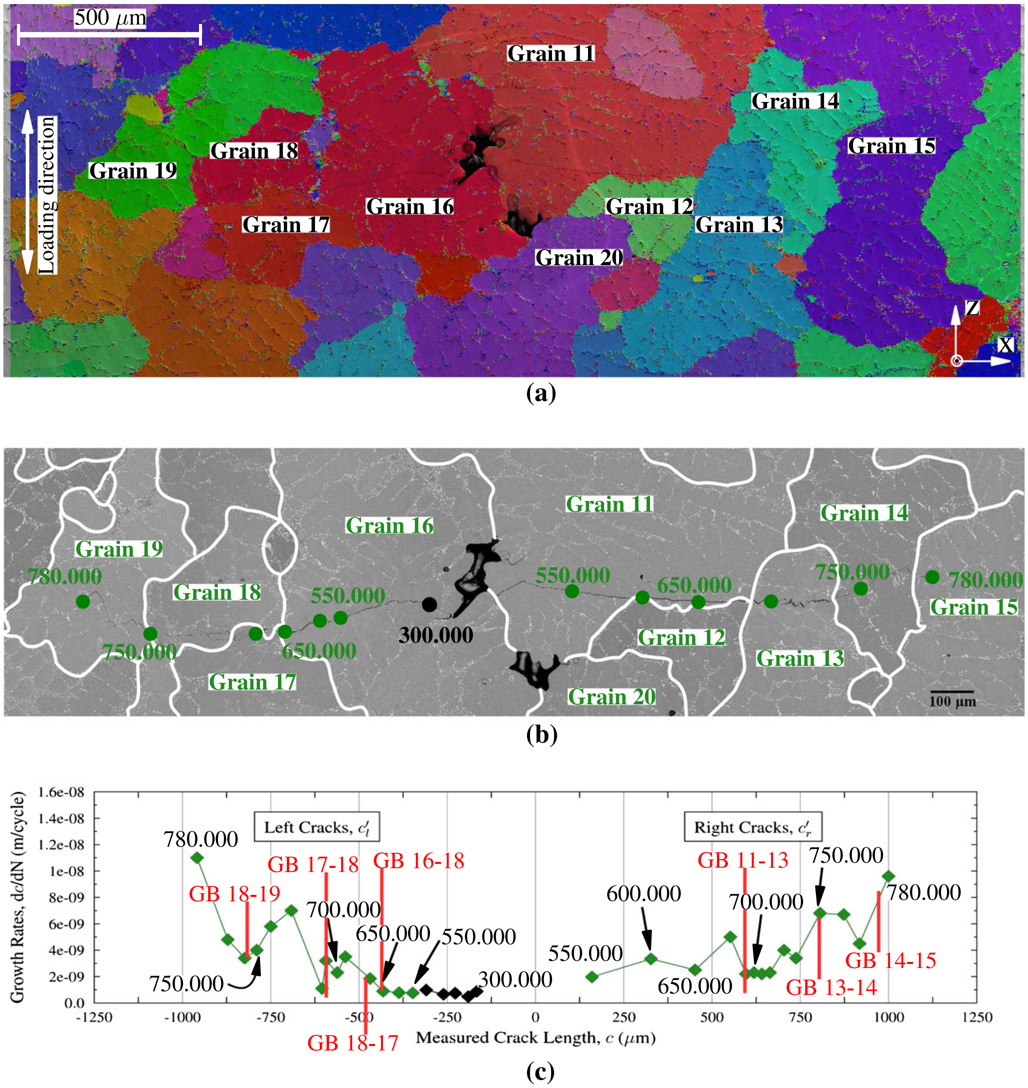

Fig. 7—(*a*) EBSD Euler map of the grain population of Sample B. The remote stress is applied along *Z*-axis. (*b*) BSE image of the crack path with green circles indicating the different stages of the propagation from 50.000 to 780.000 cycles. The white lines correspond to the approximate location of grain boundaries. (*c*) Plot of the crack growth rates d*c*/d*N* against the measured crack lengths *c*. The black diamonds from 300.000 to 500.000 cycles indicate the stages where crack propagation was only observed on the left side.

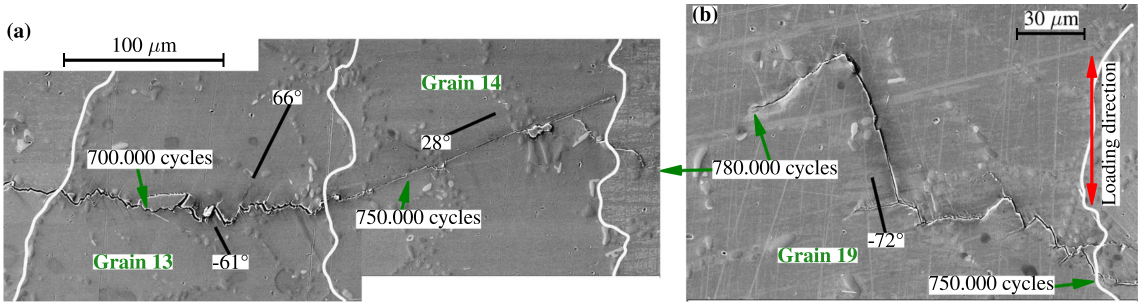

Fig. 8—Secondary electron SEM images showing (*a*) the propagation of c_{r4}' crack through Grains 13 and 14 and (*b*) the propagation of c_{l2}' crack through Grain 19. The black lines indicate the orientation of slip planes.

size, the crack is not readily formed all around Pore 2 (only crack c_{l1}' is visible on the left side). The enclosing of Pore 2 could occur during the 550.000 cycles needed for c_{r4}' crack to start propagation on the right side. The crack-enclosing of a pore has been reported in the literature for an AlSi cast alloy using *in situ* fatigue testing synchrotron tomography.[22]

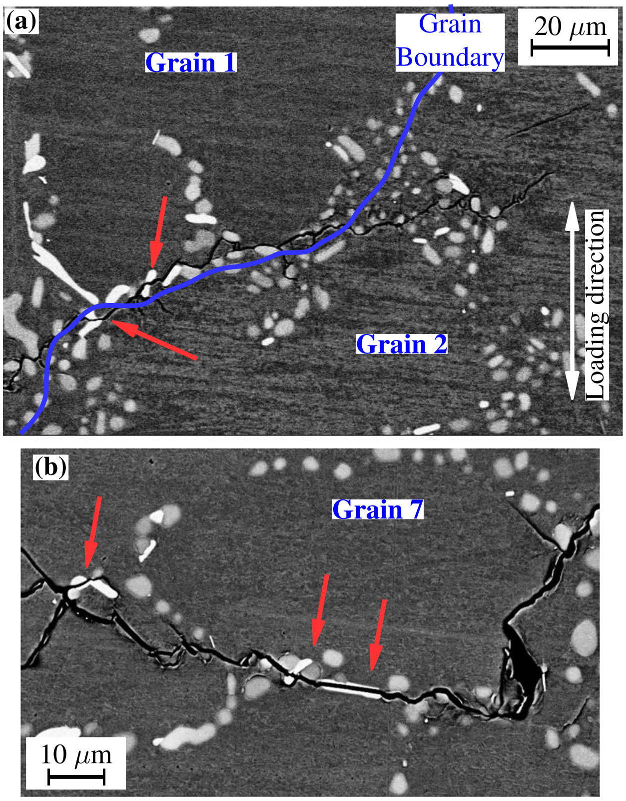

Fig. 9—(*a*) High-resolution BSE image of Crack A at the boundary between Grains 1 and 2 showing some intermetallic particles cracking (red arrows). Fe-rich intermetallic particles are shown in white, Si particles in light gray and the α-Al matrix in dark gray. (*b*) High-resolution BSE image of Crack A within Grain 7 (Color figure online).

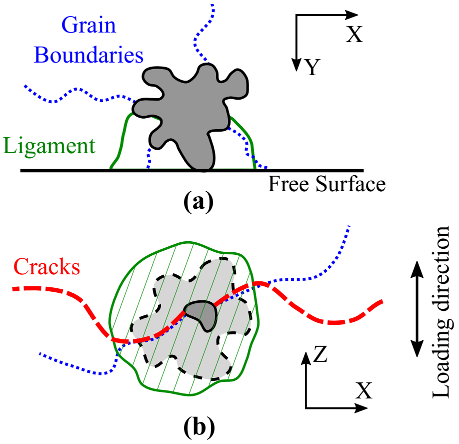

Fig. 10—Schematic illustration of crack nucleation occurring at a shrinkage porosity (*a*) as seen on *XY* plane and (*b*) as seen on *ZX* plane.

- Pore 3 seems harmless to the fatigue life, at least at the studied remote stress level. It nucleates a crack (Figure 11(c)) that is arrested after 150.000 cycles. Non-propagating cracks surrounding *small* pores ($\sqrt{A} = 100\,\mu$m) have been reported by Reference [6]. It could be argued that Pore 3 is below the critical size where fatigue life starts to be limited by other microstructural features such as Fe-rich intermetallic particles.

Note that the Kitagawa–Takahashi of the investigated material predicts propagating cracks for Pores 1 and 2 (the reader is referred to Reference 49 for further details on the Kitagawa–Takahashi diagram). It is also noteworthy that, in the two samples, the propagation distance before encountering the first grain boundaries ranges between ~ 500 and 900 μm; at these distances, the cracks have already evolved into PSC/LC. Further understanding of the role of the crystallography in small crack propagation requires the generation of more statistics (*i.e.*, specimens tested at different load and frequency levels, as well as at different stress ratios), which will lead to the manufacturing of μCT screened specimens containing artificially machined defects of controlled size and morphology.

A. *Role of the Crystallography in Nucleation and Small Crack Propagation*

The above results indicate that the intergranular cracking is confined to the vicinity of the pore and seems to play a weakening role (Figure 10). 2D FE simulations using the EBSD images are performed to gain further understanding of the role of crystallography (the remote boundary conditions is equivalent to 1 pct tensile strain; see Section II–B for more details on the CPFEM simulations). For the sake of simplicity, the simulation results are shown only for Sample A, where the intergranular cracking is most noticeable (see Figure 12). Stress concentration is observed along the grain boundaries of c_{l1}, c_{l2}. and c_{r1}, although the highest stress concentrations do not necessarily always correspond to the location of the cracks (case of c_{l2}). Moreover, the stress concentration values occurring at these grain boundaries are not the overall highest. For instance, similar stress concentration values are observed within Grain 3. Note that this 2D simulation is not able to consider the stress-raising effect induced by the ligament[50,51] (the outline of the underlying pore is shown with a white line in Figure 12). Thus, it could be that the stress level is further intensified within the ligament region, leading to higher stress localizations than the CPFEM simulation Figure 12 is able to predict. Thus, the fact of having grain boundaries arranged perpendicular to the loading direction and located within the ligament could suffice for intergranular cracking to occur during the first stages of the fatigue life of Sample A. The complete elucidation of the mechanisms leading to intergranular cracking will require the use of 3D techniques such as EBSD serial sectioning or diffraction contrast tomography combined with phase-contrast tomography.

In order to understand the influence of crystal orientation on small crack propagation, the variation in Schmid factor (SF) was analyzed for each of the cracked grains (see Figure 13). Considering the crack path topography and Schmid results, three different categories can be established: (i) SF close to 0.5 ($\gtrsim 0.48$) leads to crystallographic propagation on a single $\{111\}$

Table I. Evolution of the Crack-Tip Plastic Zone Size for Samples A and B Cracks at Different Number of Cycles

Sample A, N_f (Cycles)	50.000	—	100.000	150.000	200.000	210.000
Sample A, r_y (μm)	—	—	34.5	50.9	76.0	86.7
Sample A, $K_{\max}$ (MPa $\sqrt{m}$)	—	—	4.05	4.92	6.01	6.42
Sample A, $2c$ (μm)	586	—	869	1276	1898	2160
Sample B, N_f (Cycles)	550.000	600.000	650.000	700.000	750.000	780.000
Sample B, r_y (μm)	22.1	30.4	37.5	49.7	66.2	81.4
Sample B, $K_{\max}$ (MPa $\sqrt{m}$)	3.24	3.8	4.22	4.86	5.61	6.22
Sample B, $2c$ (μm)	558	764	943	1248	1655	2030

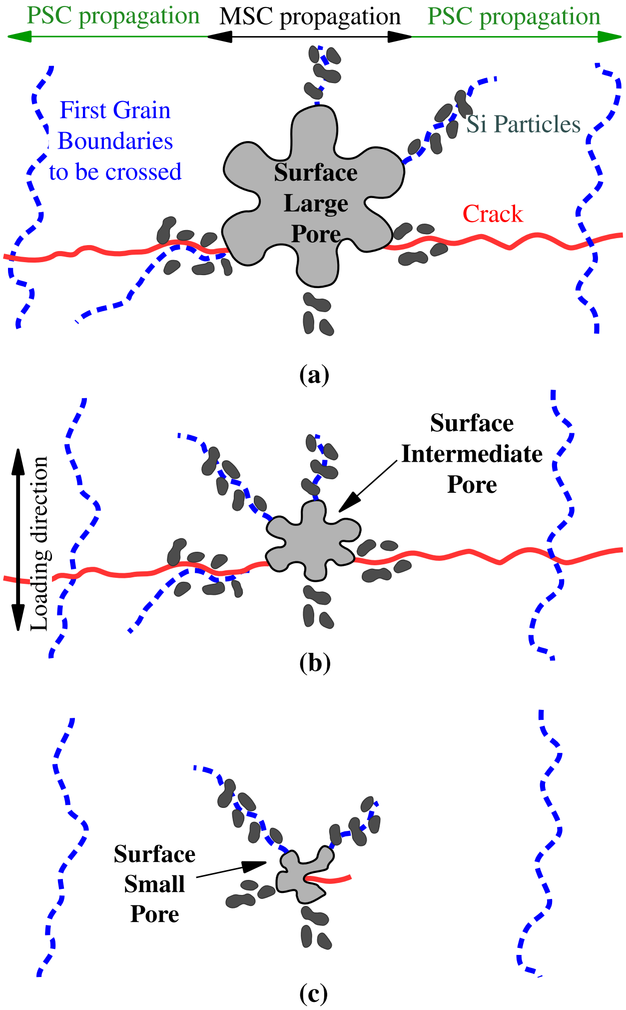

Fig. 11—Schematic illustration of the small crack propagation stages for (*a*) a *large* shrinkage pore that suppresses the MSC propagation stage is intercepting the free surface, (*b*) an *intermediate* surface pore that allows some MSC propagation to occur, and (*c*) a *small* surface pore that nucleated an non-propagating crack.

slip plane. This is the case of Grain 14 (SF = 0.48), where a relatively fast crack growth rate across the grain was observed on the slip plane at 28 deg, which corresponds to the slip plane with the highest slip activity ($\tau/\tau_c = 1.017$). (ii) Intermediate SF values ($\approx$ 0.48 to 0.4) lead to mode I-like crack paths, where no clear crystallographic features can be observed. It seems that the crystallographic orientations corresponding to the intermediate SF values allow the activation/alternation of several slip systems and, as a result, the crack path manifests as non-crystallographic. (iii) Low SF values (0.4), corresponding to Grains 13 and 19, produce rough and/or serrated crack paths with crystallographic features and the slip activity is restrained to two or three {111} planes (those where τ/τ_c ranges between 0.98 and 0.826).

The results presented in this study point at the possibility of increasing small crack growth resistance by reducing the average grain size. Literature shows that grain refinement can be achieved in AlSi cast alloys by adding grain inoculators (*e.g.*, Nb-B or Ti-B[52–54]) without greatly affecting the SDAS. Nevertheless, caution must be taken when reducing the average grain size in defect-containing materials such as cast alloys, where the ratio between the largest defect and grain size should be kept below one.[27] Improving the largest defect to grain size ratio should have two beneficial effects: first, smaller grain sizes would lead to shorter glide lengths, therefore restraining the slip activity; and second, it would also increase the probability of small crack growth getting hindered by grain boundaries. It has been shown, in aluminum wrought materials, that grain boundaries can have a significant influence on MSCs.[55,56] Note that an increased number of grain boundaries would barely influence the fatigue life of Sample A, where the small crack nucleated from Pore 1 is already evolving into a LC (see Figure 11(a)). With this view, what could be the optimal defect to grain size ratio for the studied material? On the condition that the material only contains *small* pores, such as Pores 2 and 3 (Figures 11(b) and (c)), and as long as the SDAS is kept constant, the further study of AlSi alloys with reduced average grain sizes (*e.g.*, down to $\mu m \varnothing_{A_{eq}} \approx$ 300-400 μm) should be encouraged to identify potential improvements leading to elevated fatigue resistance properties.

On a final note, it is interesting to recall that the unfavorable orientation of Grain 13 is able to slightly reduce the crack growth rates. Also, Grain 13 and particularly Grain 19 exhibit irregular/serrated crack paths that contribute to increase the overall crack path roughness. Irregular crack paths are generally associated with higher crack growth resistance, as the surface roughness is able to induce crack closure effects.[57,58]

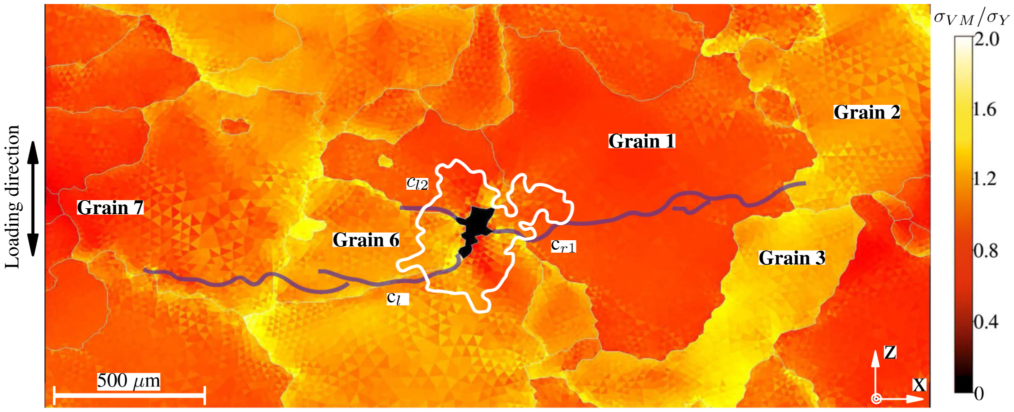

Fig. 12—CPFEM *normalized stress* $\sigma_{\mathrm{VM}}/\sigma_{\mathrm{Y}}$ calculation for Sample A. The crack path is schematically shown by blue lines and the outline of the underlying Pore 1 is shown in white.

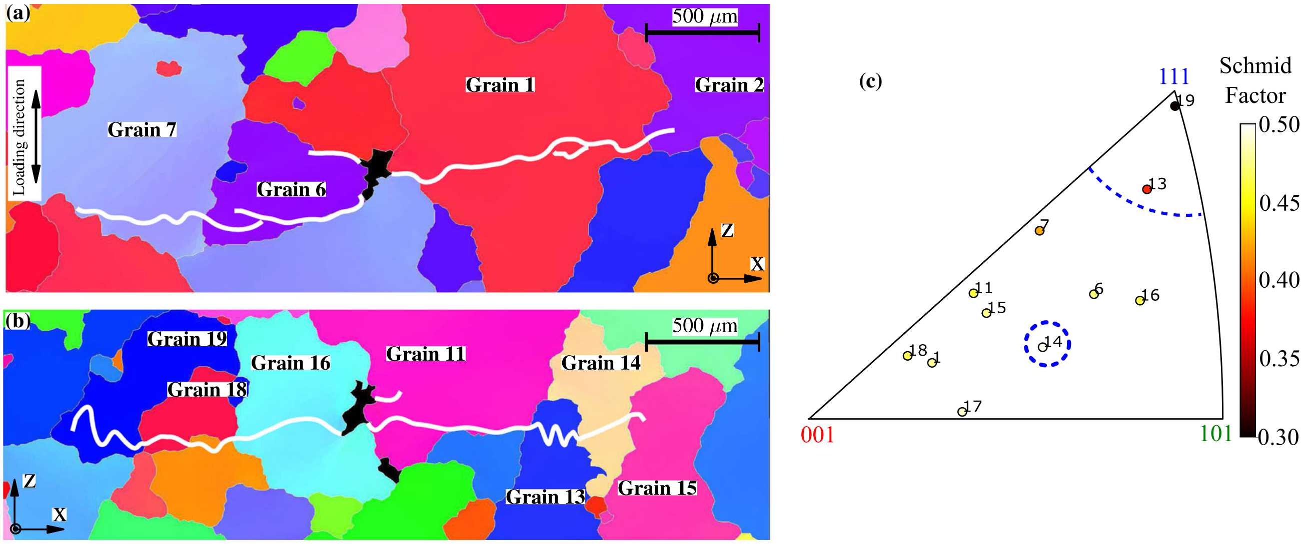

Fig. 13—Crystal orientation maps with respect to *Z*-axis for (*a*) Sample A, where Crack A is schematically shown in white, and (*b*) for Sample B. (*c*) Inverse pole figure for the loading direction with Schmid factors coloring. Dashed blue lines indicate the approximate boundaries between propagation and feature regions (Color figure online).

Thus, it could also be envisaged to tailor (*e.g.*, by directional solidification processing) the crystallographic orientation in order to increase the fatigue resistance.

V. CONCLUSIONS

The influence of pore size and microstructure on the first stages of $R = 0.1$ HCF crack propagation (*i.e.*, N_{MSC} and N_{PSC}) of an A357-T6 cast aluminum alloy has been investigated *via* laboratory X-ray μCT and microscopy (optical crack monitoring, SEM and EBSD analyses). The following conclusions can be drawn:

(1) A pore almost double the size (Pore 1 $\sqrt{A} = 522\,\mu$m against Pore 2 $\sqrt{A} = 280\,\mu$m) needs 500.000 cycles less to propagate a crack of $2c \approx 2000\,\mu$m length.

(2) Pore 1 almost suppresses both N_{N} and N_{MSC} propagation stages while Pore 2 mostly reduces N_{N}.

(3) Intergranular crack propagation is sometimes observed after nucleation and during the first stages of propagation and seems to be mainly related to the high stress levels occurring within the ligament. This point needs further investigation.

(4) The transition from N_{MSC} to N_{PSC} propagation occurs between $2c = 500$ and $550\,\mu$m. The calculation of the maximum size of the plastic zone indicates (r_{y}) suggesting that this transition corresponds to the stage where the plastic zone becomes larger than the average SDAS value $(38\,\mu$m).

(5) The crack propagation length before encountering the first grain boundaries varies between $2c \approx 500$ and $\approx 1000\,\mu$m.

(6) During N_{PSC} propagation, the crystallography is still able to induce some deceleration on the crack growth rates.

(7) The crystal orientation seems to control the crack path topography, with low SFs (SF0.4) leading to irregular/serrated crack paths.

ACKNOWLEDGMENTS

Authors thank the French National Research Agency (ANR) for the funding of this Project: "Influence des DEfauts de Fonderie sur la Fatigue des Alliages Aéronautiques" (IDEFFAAR ANR-10-RMNP-0016).

REFERENCES

1. M.J. Couper, A.E. Neeson, and J.R. Griffiths: *FFEMS*, 1990, vol. 13, p. 213.
2. B. Skallerud, T. Iveland, and G. Haerkegard: *Eng. Fract. Mech.*, 1993, vol. 44, p. 857.
3. J. Odegård and K. Pedersen: Technical Paper 940811, SAE International, 1994.
4. B. Zhang, D. Poirier, and W. Chen: *Mater. Sci. Eng. A*, 1999, vol. 30, p. 2659.
5. Q. Wang, D. Apelian, and D. Lados: *J. Light Met.*, 2001, vol. 1, p. 73.
6. J.Y. Buffiere, S. Savelli, P. Jouneau, E. Maire, and R. Fougeres: *Mater. Sci. Eng. A*, 2001, vol. 316, p. 115.
7. H. Mayer, M. Papakyriacou, B. Zettl, and S. Stanzl-Tschegg: *Int. J. Fatigue*, 2003, vol. 25, p. 245.
8. Y.X. Gao, J.Z. Yi, P.D. Lee, and T.C. Lindley: *FFEMS*, 2004, vol. 27, p. 559.
9. J. Yi, P. Lee, T. Lindley, and T. Fukui: *Mater. Sci. Eng. A*, 2006, vol. 432, p. 59.
10. H. Ammar, A. Samuel, and F. Samuel: *Mater. Sci. Eng. A*, 2008, vol. 473, p. 65.
11. X. Zhu, A. Shyam, J. Jones, H. Mayer, J. Lasecki, and J. Allison: *Third Int. Conf. Very High Cycle Fatigue (VHCF-3)*.
12. P. Li, P. Lee, D. Maijer, and T. Lindley: *Acta Mater.*, 2009, vol. 57, p. 3539.
13. M. Brochu, Y. Verreman, F. Ajersch, and D. Bouchard: *Int. J. Fatigue*, 2010, vol. 32, p. 1233.
14. N. Vanderesse, E. Maire, A. Chabod, and J.Y. Buffiere: *Int. J. Fatigue*, 2011, vol. 33, p. 1514.
15. I. Serrano-Munoz, J.Y. Buffiere, C. Verdu, Y. Gaillard, P. Mu, and Y. Nadot: *Int. J. Fatigue*, 2016, vol. 82, p. 361.
16. S. Suresh: *Fatigue of Materials*, 2nd ed., Cambridge University Press, Cambridge, 2003.
17. J. Schijve: *Fatigue of Structures and Materials*, Springer, Dordrecht, 2009.
18. A. Pineau, D.L. McDowell, E.P. Busso, and S.D. Antolovich: *Acta Mater.*, 2016, vol. 107, p. 484.
19. D. McDowell, K. Gall, M. Horstemeyer, and J. Fan: *Eng. Fract. Mech.*, 2003, vol. 70, p. 49.
20. T. Zhai, A. Wilkinson, and J. Martin: *Acta Mater.*, 2000, vol. 48, p. 4917.
21. W. Ludwig, J. Buffiere, S. Savelli, and P. Cloetens: *Acta Mater.*, 2003, vol. 51, p. 585.
22. E. Ferrie, J.Y. Buffiere, and W. Ludwig: *Int. J. Fatigue*, 2005, vol. 27, p. 1215.
23. W. Schaef, M. Marx, H. Vehoff, A. Heckl, and P. Randelzhofer: *Acta Mater.*, 2011, vol. 59, p. 1849.
24. S. Siegfanz, A. Giertler, W. Michels, and U. Krupp: *Mater. Sci. Eng. A*, 2013, vol. 565, p. 21.
25. U. Krupp, A. Giertler, S. Siegfanz, and W. Michels: *Key Eng. Mater.*, 2013, vol. 592, p. 393.
26. K.J. Miller: *Fatigue Eng. Mater. Struct.*, 1982, vol. 5, p. 223.
27. K.J. Miller: *Mater. Sci. Technol.*, 1993, vol. 9, p. 453.
28. K. Shiozawa, Y. Tohda, and S.M. Sun: *FFEMS*, 1997, vol. 20, p. 237.
29. Y. Murakami and M. Endo: *Int. J. Fatigue*, 1994, vol. 16, p. 163.
30. I. Serrano-Munoz, J.Y. Buffiere, and C. Verdu: *Int. J. Fatigue*, 2018, vol. 117, p. 471.
31. I. Serrano-Munoz, J.Y. Buffiere, R. Mokso, C. Verdu, and Y. Nadot: *Sci. Rep.*, 2017, vol. 7, p. 45239.
32. Q. Wang, D. Apelian, and D. Lados: *J. Light Met.*, 2001, vol. 1, p. 85.
33. K. Gall, N. Yang, M. Horstemeyer, D.L. McDowell, and J. Fan: *FFEMS*, 2000, vol. 23, p. 159.
34. R. Carter, E. Lee, E. Starke, and C. Beevers: *Metall. Trans. A*, 1984, vol. 15, p. 555.
35. J. Schindelin, I. Arganda-Carreras, E. Frise, V. Kaynig, M. Longair, T. Pietzsch, S. Preibisch, C. Rueden, S. Saalfeld, B. Schmid, J.Y. Tinevez, D.J. White, V. Hartenstein, K. Eliceiri, P. Tomancak, and A. Cardona: *Nat. Methods*, 2012, vol. 9, p. 676. EP Perspective.
36. ARP1947A: *Aerospace Recommended Practice*, SAE International Group, 2007.
37. HKL-Technology: *HKL Channel 5 Users Manual*, HKL-Technology, Danbury, CT, 2001.
38. I. Serrano-Munoz: Influence of Casting Defects on the Fatigue Behaviour of an A357-T6 Aerospace Alloy. Ph.D. Thesis, INSA de Lyon, 2014.
39. P. Van Houtte, S. Li, M. Seefeldt, and L. Delannay: *Int. J. Plast.*, 2005, vol. 21, p. 589.
40. L. Delannay, M. Melchior, J. Signorelli, J.F. Remacle, and T. Kuwabara: *Comput. Mater. Sci.*, 2009, vol. 45, p. 739.
41. S. Dancette, L. Delannay, T. Jodlowski, and J. Giovanola: *Int. J. Mater. Form.*, 2010, vol. 3, p. 251.
42. S. Dancette, L. Delannay, K. Renard, M. Melchior, and P. Jacques: *Acta Mater.*, 2012, vol. 60, p. 2135.
43. S. Dancette, A. Browet, G. Martin, M. Willemet, and L. Delannay: *Model. Simul. Mater. Sci. Eng.*, 2016, vol. 24, p. 055014.
44. L. Delannay, P.J. Jacques, and S.R. Kalidindi: *Int. J. Plast.*, 2006, vol. 22, p. 1879.
45. C. Lavogiez, S. Dancette, S. Cazottes, C. Le Bourlot, and E. Maire: *Mater. Charact.*, 2018, vol. 146, p. 81.
46. J. Campbell: *Casting Practice: The Ten Rules of Casting*, Butterworth-Heinemann, Oxford, 2004.
47. T.L. Anderson: *Fracture Mechanics*, CRC Press, Boca Raton, 1995, p. 627.
48. J. Newman, Jr. and I. Raju: *Eng. Fract. Mech.*, 1981, vol. 15, p. 185.
49. P. Mu, Y. Nadot, C. Nadot-Martin, A. Chabod, I. Serrano-Munoz, and C. Verdu: *Int. J. Fatigue*, 2014, vol. 63, p. 97.
50. Z. Xu, W. Wen, and T. Zhai: *Metall. Mater. Trans. A*, 2012, vol. 43A, p. 2763.
51. A. Borbely, H. Mughrabi, G. Eisenmeier, and H. Hoppel: *Int. J. Fract.*, 2002, vol. 115, p. 227.
52. L. Bolzoni, M. Nowak, and N.H. Babu: *Mater. Des. (1980–2015)*, 2015, vol. 66, p. 376.
53. S. Nafisi and R. Ghomashchi: *J. Mater. Process. Technol.*, 2006, vol. 174, p. 371.
54. E. Samuel, B. Golbahar, A. Samuel, H. Doty, S. Valtierra, and F. Samuel: *Mater. Des. (1980–2015)*, 2014, vol. 56, p. 468.
55. C.Y. Kung and M.E. Fine: *Metall. Trans. A*, 1979, vol. 10, p. 603.
56. W.L. Morris: *Metall. Trans. A*, 1980, vol. 11, p. 1117.
57. J. Schijve: *Eng. Fract. Mech.*, 1981, vol. 14, p. 467.
58. R. Ritchie: *Workshop Mech. Phys. Crack Growth Appl. Life Predict*.